Effect of Back Pressure and Divergence Angle on Location of Normal Shock Wave

Fatma A-M. Kassem[1*], Mohamed R. A. Shaalan[2], Reham S. Hegazy[3], Saeed A. A. Ibrahim[2]

[1] Volume and Fluid Flow Metrology Laboratory, National Institute of Standards (NIS)
[2] Mechanical Power Engineering, Faculty of Engineering, Zagazig University
[3] Force and Material Metrology Laboratory., National Institute of Standards (NIS)

*Corresponding author's email: fatma.abdelmordy@nis.sci.eg

Abstract

This paper presents a study of the effect of back pressure variation on the mass flow rate and normal shock occurrence in a sonic nozzle. ANSYS-FLUENT software was used for numerical simulation, and experimental measurements were carried out to verify the numerical results. Nozzles of various designs (different divergence angles and throat diameters) were subjected to investigation. The simulation results indicate that both the divergence angle and the throat diameter markedly influence the performance via the occurrence of normal shock in the divergent part of the nozzle. The nozzle throat diameter ranges from 0.558 to 3.175 mm, and the back-pressure ratio is 0.6. Normal shocks move toward the nozzle exit upon a decrease in divergence angle and an increase in throat diameter. For this diameter range, the corresponding distance from the nozzle inlet toward the divergent section at which a normal shock occurs is 2.8 to 3.2.

Nomenclature

A_{th}	Venturi throat area	m^2	u_x	Axial component of velocity	$m\ s^{-1}$
C^*	Critical flow factor $C^* = \sqrt{\gamma}\left(\frac{\gamma+1}{2}\right)^{\frac{\gamma+1}{2(1-\gamma)}}$	-	v_r	Radial component of velocity	$m\ s^{-1}$
C_d	Discharge coefficient	-	x	Axial coordinate	m
d	Throat diameter	m	T	Temperature	K
K	Coverage factor	-	**Greek symbols**		
M	Mach number	-	θ	Divergent angle	Deg.
P	Pressure	Pa	γ	Specific heat ratio	-
P_s	Static pressure	Pa	δ	Thickness boundary layer	m
q_m	Real mass flow rate	$kg\ sec^{-1}$	μ	Dynamic viscosity	Pa.s
$q_{m,\ ref}$	Mass flow rate being chock	$kg\ sec^{-1}$	ρ	Density	$kg\ m^{-3}$
R	Gas constant	$J\ kg^{-1}\ K^{-1}$	τ	Shear stress	$N\ m^{-2}$
Re	Reynolds number $= \frac{4q_m}{\pi d_{th}\mu}$	-	**Subscripts**		
r	Radial coordinate	m	o	Stagnation condition	
S	Entropy	$J\ kg^{-1}\ K^{-1}$	1	Condition before the normal shock wave	
U	Expanded uncertainty	$kg\ sec^{-1}$	2	Condition after normal shock wave	
u_c	Combined uncertainty	$kg\ sec^{-1}$	th	Throat condition	

1   Introduction

Sonic nozzles are effective reference flow metres that can be used to calibrate other devices. They can also be a fundamental part of a primary standard. They are mentioned specifically due to their extensive use as the calibration reference standard in many applications and laboratories. Although not a primary method of calibration, a sonic nozzle can be part of a system when combined with primary methods. Sonic nozzles provide the reference system for many calibration facilities, where their stability requires infrequent calibration of the nozzle to meet the performance outlined in documentary standards.

If the pressure drop between the inlet and the throat of a nozzle or restriction is increased, the flow rate rises until the sonic velocity is reached at the throat. At this point, the nozzle is choked and the mass flow rate through the nozzle increases with the upstream pressure increment according to eqn. (1). Growth of the boundary layer on the nozzle wall affects the outlet condition and thus causes a normal shock to occur in the divergent part of the nozzle. An almost spontaneous change from supersonic flow to subsonic flow then takes place. Such normal shocks are expected to influence the nozzle performance in terms of mass flow rate, hence the discharge coefficient.

An overexpansion usually occurs because the nozzle outlet pressure is below the atmospheric pressure when the nozzle has too large an area-expansion ratio or a low nozzle pressure ratio, as described by Sutton [1]. In the case of high overexpansion, the exhaust jet of the supersonic nozzle separates from the nozzle wall because of the large adverse pressure gradient. Correspondingly, to match the pressure of the separated flow region, an oblique shock is generated, which evolves through the supersonic jet starting around the separation point of Nasuti and Marcello [2]. In addition, the rise of gas pressure at the nozzle outlet to atmospheric pressure also causes normal-shock waves, causing a loss of thrust performance. In rocket design, shock-induced separation is considered undesirable because an asymmetry in the flow can yield dangerous additional forces, which may damage the nozzle. Choi et al. [3].

$$q_m = C_d \ C* \ A_{th} \ P_o \ \frac{1}{\sqrt{R \ T_o}} \tag{1}$$

Jae et al. [4], Shaalan et al. [5], and Park et al. [6] studied experimentally the effect of the critical pressure ratio of a sonic nozzle on the ratio of flow rate at different angles in the range of 2° to 8° and various throat diameters in the range of 0.28 to 4.48 mm with Reynolds number below 105. The results agree with ISO 9300 [7] for divergence angle range 2° to 6°, whereas, for the angle 8°, a decrease of 5.5% is observed with uncertainty $\pm$ 3.2% at coverage factor (k= 2). Also developed a transfer standard system with sonic Venturi nozzles for calibrating small mass flow rates of gases in the range from 10 mg/min to 100 g/min with the expanded standard uncertainty (k= 2) being less than 0.2% for N_2 by Masao et al. [8].

Ke et al. [9] gave a numerical simulation study of the internal flow field downstream of a sonic nozzle and its effect on the discharge coefficient. The pressure drops significantly from the nozzle outlet and after a distance of about 3D (Pipe diameter), the pressure rises to the back pressure. But at distance 5D the nozzle keeps critical condition when the back-pressure ratio is below 0.849. Kim et al. [10] presented a numerical simulation of divergence angle and throat diameter as they affect the mass flow flux through the nozzle at a throat diameter range of 0.2 to 2 mm and divergence angle range of 2° to 8°.

Previous studies have clarified that the divergence angle affects mass flow flux. Also, the discharge coefficient of the toroidal sonic nozzle is more dependent on the Reynolds number based on velocity at the throat diameter of the nozzle Geropp [11], and Arnberg et al. [12]. When the Reynolds number is increased, the discharge coefficient is found to be increasing correspondingly due to the nozzle reaching to choked condition at the throat, however a lower Reynolds number, the discharge coefficient is decreased Stratford [13] due to the wall boundary layer effects on mass flow rate across the sonic nozzle.

Liu et al. [14] studied the boundary separation across normal shock waves using a Laval nozzle. The results explain why the length of the boundary separation interval decreases with a decrease in the upstream Mach number. Balasubramanian and Lee [15] explained the effects of the divergence angles on the condensation phenomena with a wet steam model in the nozzle. According to the results, the condensation shock captured near the throat of the nozzle is stronger, and the aerodynamic shock moves downstream as the divergence angle is decreased. In addition, the static temperature of the flow is increased due to the addition of latent heat.

In this study, four sonic nozzles with different diameters will be tested and evaluated experimentally and numerically under different conditions (Nozzle Pressure Ratio) to assess factors concerning the location of normal-shock waves to avoid. To prevent separation of the flow inside the nozzle, as a result of reverse pressure created by the normal-shock wave.

2 Numerical work

2.1 Governing Equations

For the present research, the flow was studied as steady, axisymmetric, two dimensions (2D), and compressible flow through a critical toroidal nozzle controlled by the Navier-Stokes equations. In this work, the fluid is assumed to be a perfect gas with a constant specific heat ratio (i.e., γ= constant) with an adiabatic wall in a computational domain. The thermal conductivity and the molecular viscosity are related to temperature by the Sutherland viscosity law. The effects of turbulence are introduced through the standard (k-ε) turbulence model. Reynolds number range is 2×10^4 to 4×10^6.

The mass conservation equations (2,3, and 4) for steady-state flow is given by ANSYS-Fluent [16]. The continuity equation is given as:

$$\frac{\partial}{\partial x}(\rho\,u_x) + \frac{\partial}{\partial r}(\rho\,v_r) = 0 \tag{2}$$

The axial and radial momentum equations are:

$$\frac{1}{r}\frac{\partial}{\partial x}(r\rho\,u_x u_x) + \frac{1}{r}\frac{\partial}{\partial r}(r\rho\,u_x v_r) = -\frac{\partial P}{\partial x} + \frac{1}{r}\frac{\partial}{\partial x}\left[r\mu\left(2\frac{\partial u_x}{\partial x} - \frac{2}{3}(\nabla.\vec{v})\right)\right] + \frac{1}{r}\frac{\partial}{\partial r}\left[r\mu\left(\frac{\partial u_x}{\partial r} + \frac{\partial v_r}{\partial x}\right)\right] \tag{3}$$

$$\frac{1}{r}\frac{\partial}{\partial x}(r\rho\,u_x v_r) + \frac{1}{r}\frac{\partial}{\partial r}(r\rho\,v_r v_r) = -\frac{\partial P}{\partial r} + \frac{1}{r}\frac{\partial}{\partial x}\left[r\mu\left(2\frac{\partial v_r}{\partial x} + \frac{\partial u_x}{\partial r}\right)\right] + \frac{1}{r}\frac{\partial}{\partial x}\left[r\mu\left(2\frac{\partial v_r}{\partial r} - \frac{2}{3}(\nabla.\vec{v})\right)\right] -$$

$$2\mu\frac{v_r}{r^2} + \frac{2}{3}\frac{\mu}{r}\frac{\partial}{\partial r}(\nabla.\vec{v}) \tag{4}$$

Where: $\nabla.\vec{v} = \frac{\partial u_x}{\partial x} + \frac{\partial v_r}{\partial r} + \frac{v_r}{r}$

2.2   Grid sensitivity

The number of grid elements is important in the computational analysis to ensure the computational accuracy of the field variables. A fine grid may require excessive amounts of computational power to obtain a solution, whereas a coarse grid may entail numerical errors and convergence problems. To test the independence of the computational results on the grid number of cells, an unstructured mesh grid was generated in the specified computational domain using CFD – Geometry software. The number of grid points affects the mass flow rate for a sonic nozzle throat diameter of 3.175 mm (see Table (1)). The results of the grid independence check over ten grid resolutions are presented. The minimum relative error of the mass flow rate at the sonic nozzle outlet between cases is 0.002957%. It could be concluded that the grid system reached an independent solution. Therefore, the grid density of 19,500 cells was found to be sufficient and applied in the ongoing study.

Table 1: *Grid independence solution*

No. of nodes × No. of elements	Mass flow rate (q_i)	Different percentage (%) $\left(\dfrac{q_{i+1} - q_i}{q_i}\right) * 100$
4,941×4,800	0.0100927	-
5,750×5,600	0.0100874	0.052513203
6,561×6,400	0.0100821	0.052540793
7,371×7,200	0.010077	0.0505847
8,991×8,800	0.0101546	0.033471156
9,801×9,600	0.0101515	0.030528037
10,611×10,400	0.0101486	0.028567207
11,421×12,200	0.0101459	0.026604655
16,231×18,000	0.0101454	0.004928099
21,041×23,500	0.0101451	0.002957005

2.3   Computational Domain and Boundary Conditions

The geometry of the critical nozzle is according to ISO 9300 [7] standards and is shown schematically in Figure (1). The nozzle consists of a converging section of inlet diameter equal to $2.5d_{th}$ with contraction of a circular arc radius= $2d_{th}$ and enters the nozzle throat at a point of tangency. At this point, the shape starts becoming conical (divergence section) of length =$7d_{th}$. At the nozzle inlet T_o and P_o were constants, and the back-pressure ratio is 0.6. Axis-symmetry flow conditions were assumed along the centerline. The computations were taken to be density based, steady. The implicit method was applied in solving the k-ε turbulent flow model. For the wall adiabatic (i.e. heat flux =0) is assumed. Figure (2) explain the numerical flow chart for the estimation of normal shock wave location inside the divergence section.
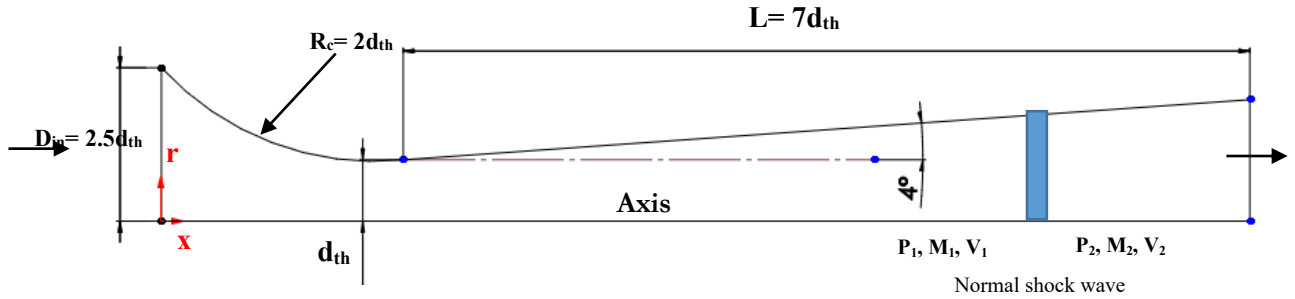
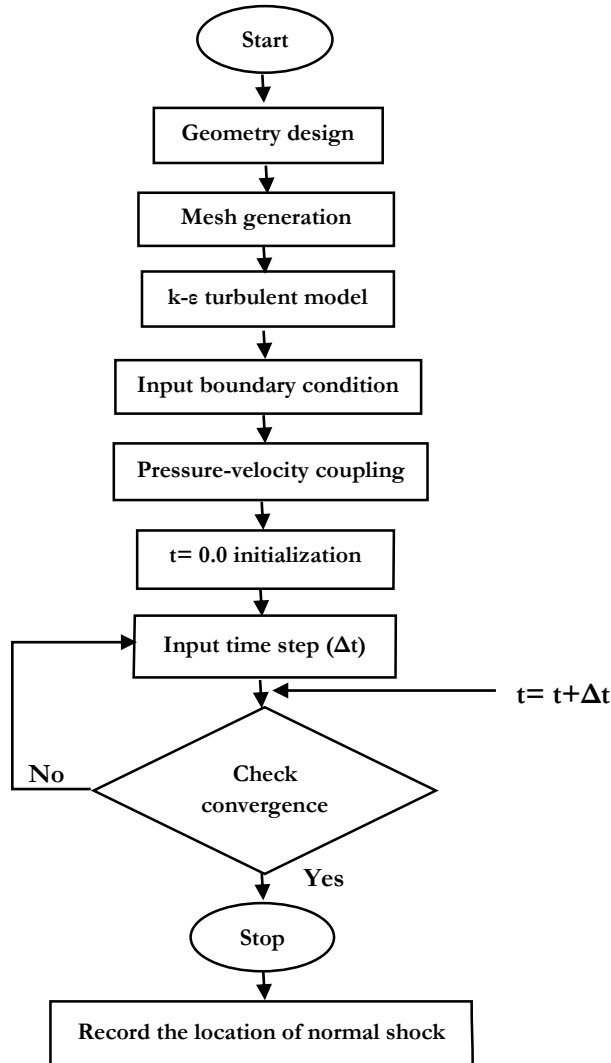**Figure 1:** Model geometry of a sonic nozzle

Figure 2: Computational flow chart for estimation of normal shock location

3 Experimental work

The main components of the test system are illustrated in Fig. 2 and described by the schematic diagram in Fig. 3, which shows the setup of the system that consists of the compressor, two air dryers, air filters, a storage tank, a pneumatic control valve, temperature sensors, two pressure gauge sensors, data acquisition, a laptop, and a sonic nozzle.

Compressed air with humidity and impurities passes through the air dryers (0.74 kW, T_{max}=120 ºC), then through the air filters. The air is then stored in a storage tank of capacity 2 m^3 and maximum permissible pressure of 10 bar. The air travels through a pipe of length of about 30 m which is long enough to stabilize temperature and pressure. The amount of air passing through the pneumatic control valve and then regulating valves control the flow depending on the mass flow rate required. Air is then allowed to flow through the sonic nozzle.
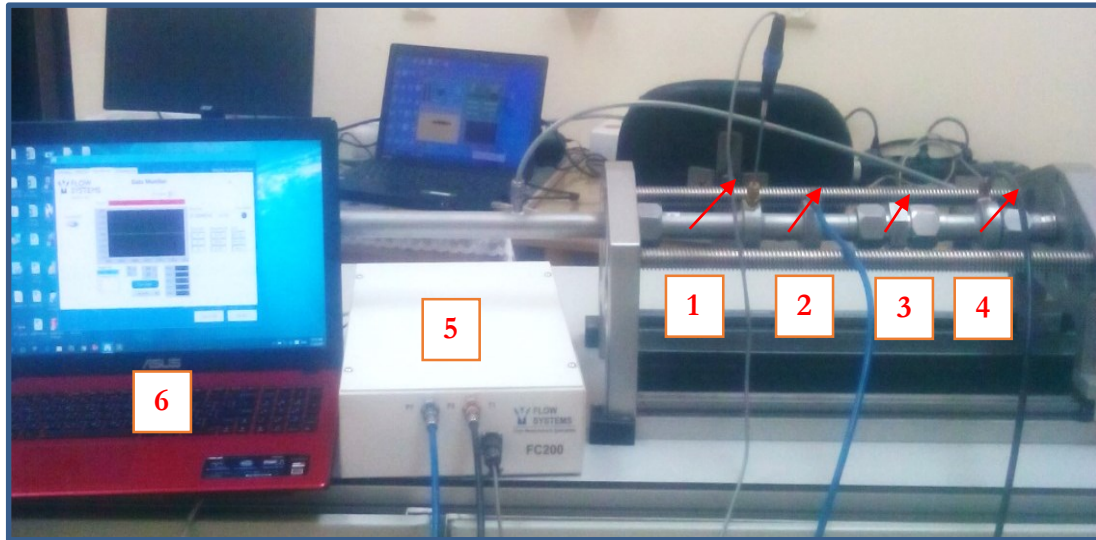
| 1 | Upstream pressure | 3 | Sonic nozzle | 5 | Data acquisition unit |
| 2 | Upstream temperature | 4 | Downstream pressure | 6 | Computer system |

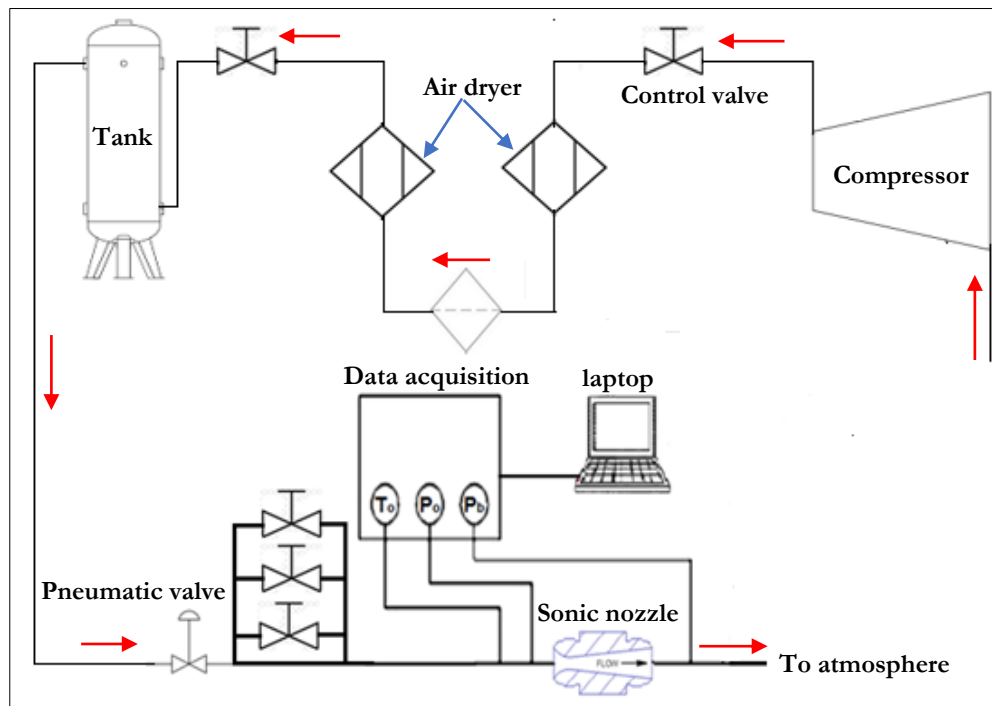**Figure 3:** Photo of sonic nozzle and software.

Figure 4: Schematic diagram of a sonic nozzle setup

3.1   Test Setup and Procedure

According to test setup components and the location of measuring points for pressures and temperatures. A typical test was run as follows:

(i)   Opening the valve before the sonic nozzle.

(ii)   Measuring upstream pressure (P_o) and temperature (T_o) by a pressure sensor and temperature sensor at an operating range from 101.3 to 600 kPa.

(iii)   Measuring downstream pressure by a downstream pressure sensor.

(iv)   Recording results translated by data acquisition by using the computer (P_o, T_o, P_b, q_m, $q_{m,\,ref}$).

(v)   Change the opening of the valve to increase the upstream pressure and start recording the readings.

(vi)   Repeat step (v).

(vii)   Calculate the ideal mass flow rate according to eqn. (5). Then calculate the discharge coefficient (C_d) by eqn. (6).

$$q_{mi} = C^* \, A_{th} \, P_o \, \frac{1}{\sqrt{R \, T_o}} \qquad\qquad (5)$$

$$C_d = \frac{q_m}{q_{mi}} \qquad\qquad (6)$$

(viii) Finding Relationship between (P_b/P_o) and ($q_m/q_{m,\,ref}$)

3.2   Measurements

The following quantities were measured in a typical test:

(i)   Upstream pressure P_o: by means of pressure sensor mounted at nozzle inlet section with uncertainty $\pm$ 0.01 kPa.

(ii)   Upstream temperature T_o: by means of a temperature sensor mounted at the nozzle exit section with uncertainty $\pm$ 0.048 ℃.

(iii) Exit (back) pressure P_b: by means of pressure sensor mounted at nozzle exit section with uncertainty $\pm$ 0.01 kPa.

(iv)   Mass flow rate: The mass flow rate was obtained from the data acquisition unit based on the eqn. (1):

(v)   Normal shock occurrence location:

It was not experimentally possible to monitor the location of normal occurrence since the setup was not equipped to measure the pressure distribution through the nozzle. The shock occurrence location was obtained from computational fluid dynamics. The above measurements were carried out for various throat diameters at a divergence angle $\theta = 4^o$.

4   Results and discussion

4.1   Validation of the numerical computations.

Figure (5) shows an experimental variation of mass flow rate with back pressure ratio for divergence angle $\theta = 4^o$, and also the corresponding computational variation for various divergence angles. It appears that the back-pressure ratio required to reach critical condition at the throat is dependent upon the angle of the divergent part (see table (2) for various angles from 2° to 6°, showing a change in the critical pressure ratio from 0.82 to 0.875. This may be attributed to the effect of the boundary layer as when the divergence angle is larger, the velocity is higher, the effect of the boundary layer

is expected to be smaller and steady flow attains the critical condition faster than with a smaller divergence angle.
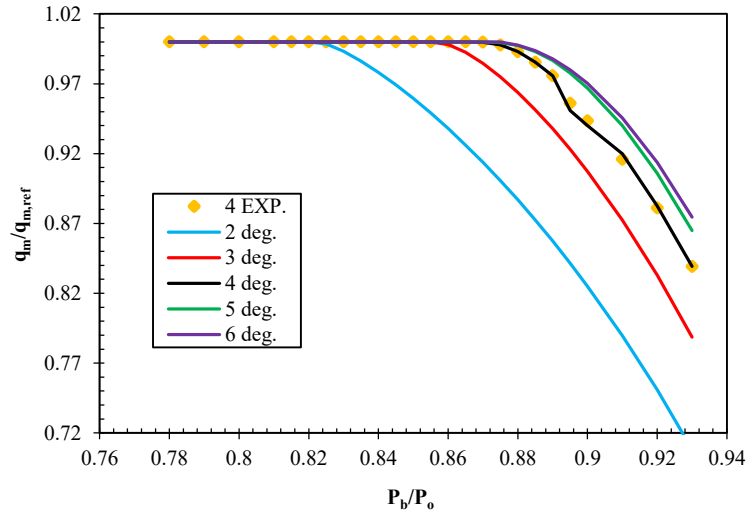

Figure 5: Effect of back pressure ratio on mass flow rate ratio for different divergence angles.

Table 2: *Critical pressure ratio for choking at the throat for different divergent angles.*

θ(deg.)	P_{cr}
2°	0.820
3°	0.845
4°	0.860
5°	0.865
6°	0.875

4.2   Effect of Reynolds number on mass flow ratio

Figure (6) clarifies the relationship between the Reynolds number and discharge coefficient. The result indicates that, the discharge coefficient is dependent on the Reynolds number and that the latter is an important factor that should be considered in the measurement of mass flow rate. As (Re_d) is increased, (C_d) gets higher. The error of the results between computations, experiments, and Ishibashi, and Takemoto [17] not exceeding 0.2 % when θ= 4°, which represents a good agreement.

4.3   Effect of back pressure ratio

Figure (7) shows the experimental variation of the back-pressure ratio on normalized mass flow rate for various throat diameters.

For a given throat diameter of 0.558mm an increase in back pressure ratio causes a decrease in mass flow rate with a constant upstream pressure P_o.   For the nozzle throat diameter range of 0.558 to 3.175mm, the pressure ratio required to reach critical condition at the throat increases from 0.84 to 0.88 nearly with air being the standard working fluid.
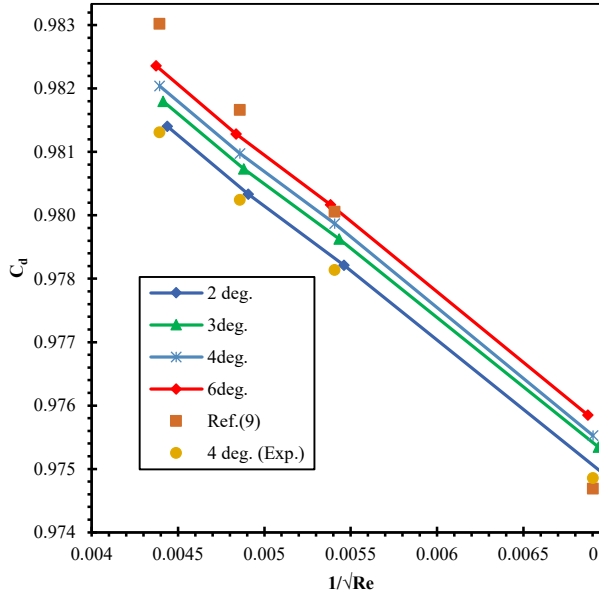
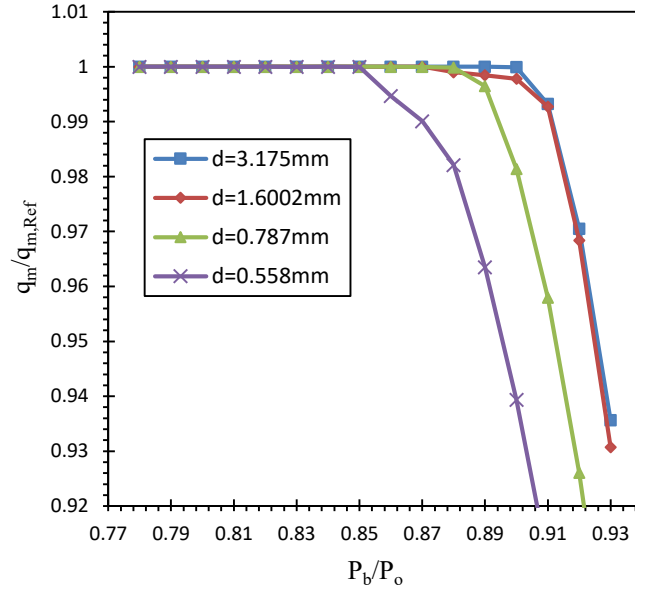**Figure 6:** C_d vs Reynolds number parameter

Figure 7: Effect of back pressure ratio on mass flow rate ratio for different throat diameters.

4.4 *Uncertainty analysis for experimental results*

The uncertainty budget measuring mass flow rate by sonic nozzle was summarized in Table (3) according to eqn. (7) with assume the discharge coefficient C_d, and R (gas constant) are constant.

$$u(q_m) = \sqrt{\left(\frac{\partial q_m}{\partial c^*}\, u(c^*)\right)^2 + \left(\frac{\partial q_m}{\partial A_{th}}\, u(A_{th})\right)^2 + \left(\frac{\partial q_m}{\partial P_o}\, u(P_o)\right)^2 + \left(\frac{\partial q_m}{\partial T_o}\, u(T_o)\right)^2} \qquad (7)$$

Table 3: *Uncertainty budget of measuring by sonic nozzle.*

Items source (x_i)	Distribution	Standard uncertainty $u(x_i)$	Divisor	Coefficient of sensitivity(c_i)	Uncertainty contribution $u= u(x_i) \times c_i$
Inlet pressure sensor P_o(kPa)	Normal	0.005	1	1.8209×10^{-8}	9.140×10^{-11}
Inlet temperature sensor T_o(K)	Normal	0.024	1	-1.536×10^{-6}	-3.687×10^{-8}
Throat diameter d_{th} (m)	Normal	2.299×10^{-6}	1	0.013	3.057×10^{-8}
Critical flow factor C*(-)	Normal	7.002×10^{-6}	1	5.735	4.015×10^{-5}
Standard uncertainty $u(q_m)$ (kg/s) = 1.319×10^{-5}					
Expanded uncertainty $U(q_m)$ (kg/s) = 2.638×10^{-5}					

4.5. *Effect of throat diameter on static pressure variation through nozzle and location of the shock*

The computed static pressure distribution along the present sonic nozzle is shown in Fig. (8). For a fixed divergence section of $\theta= 4^o$, L= $4d_{th}$, back pressure ratio 0.6, and various throat diameters in the range 0.558 to 3.175 mm, with d_{th} =0.5588 mm, the flow is accelerated to the minimum nozzle area (throat) (X/d= 1.12), then supersonic flow changes path caused by normal shock near X/d=2.8,

leading to the static pressure jumps. After the pressure jump, the flow is decelerated to subsonic speed, equaling the boundary condition set at the nozzle exit.
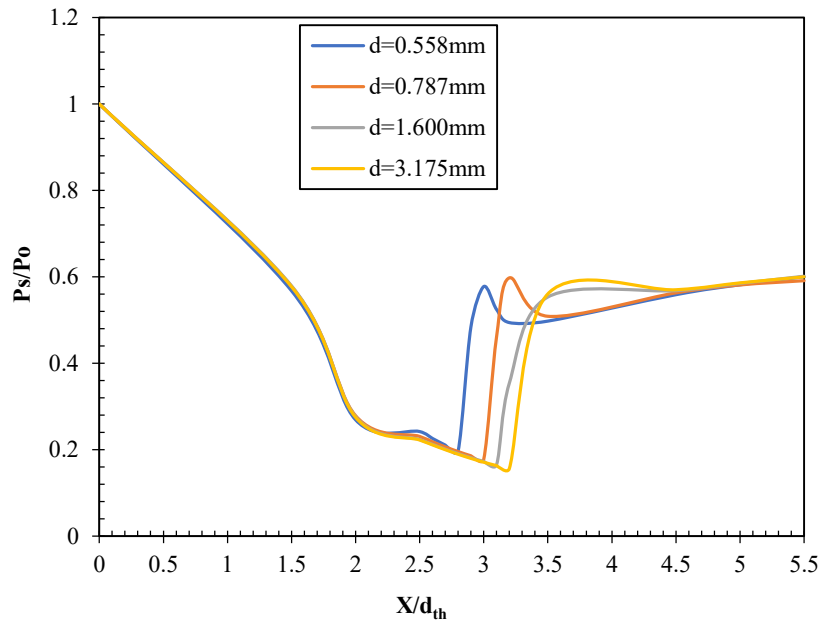

Figure 8: Static pressure distributions along the sonic nozzle in the presence of normal shock for various throat diameters and the same divergence angle (θ =4º).

As the throat diameter is decreased, the normal shock moves closer to the nozzle throat (Table (4)). It is clear that the pressure jump moves upstream a little with decreased throat diameter. This is due to the effect of the wall boundary layer relative to the diameter of the nozzle.

Table 4: *Local distance of shock for nozzles of various diameters.*

d(mm)	X/d
0.5588	2.8
0.7870	3.0
1.6002	3.1
3.1750	3.2

4.5   Effect of divergence angle on static pressure variation and location of the shock

The effect of the divergence angle on pressure variation through a nozzle under shock is shown in Fig. (9) and Table 5. The static pressure distributions for a case of d_{th}= 3.175 mm are presented. It is clear that the flow expands more rapidly to the throat as the divergence angle is increased, reaching the normal shock condition. For θ= 6º, it appears that the flow shocked faster than for θ= 4º, θ= 3º, and θ =2º.

While Fig. (9b) similar trend compared to Fig. (9a), some differences are found in the trend. This is because area increases; therefore, the boundary effect is relatively reduced in larger critical nozzles, due to velocity increases.

Table 5: *Locations of normal shock for various divergence angles.*

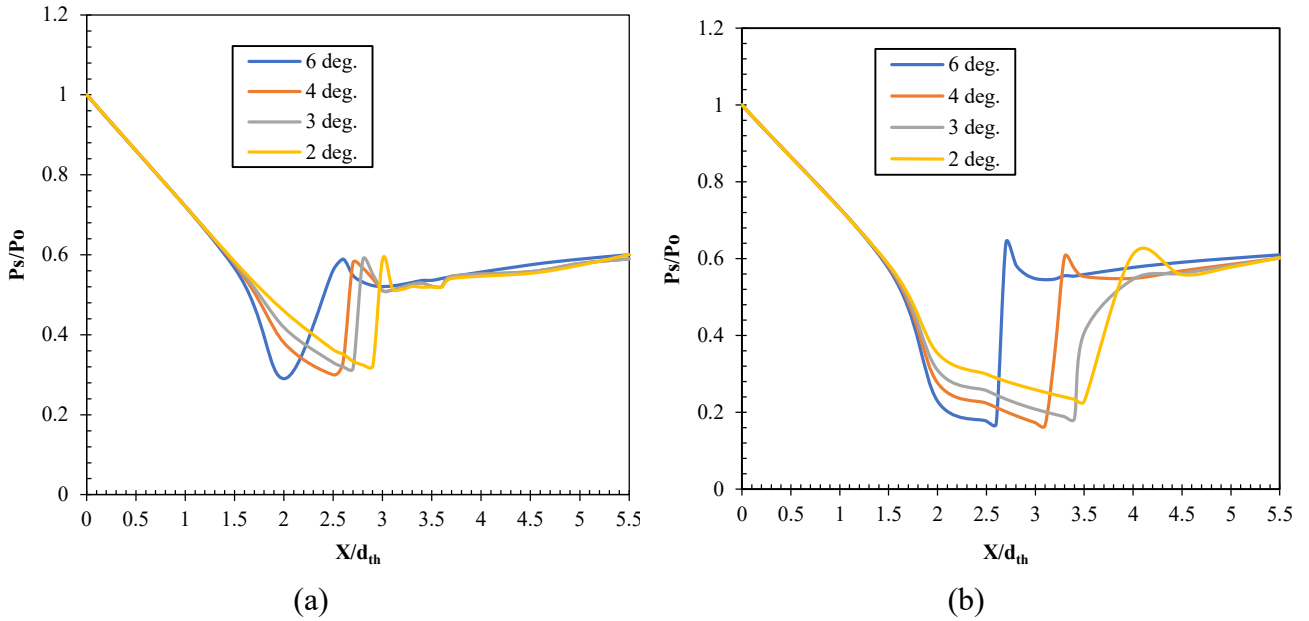| Angle (deg)	X/d (at normal shock)	
	d= 0.5588 mm	d= 3.175 mm
6º	2.0	2.5
4º	2.5	3.1
3º	2.7	3.4
2º	2.9	3.5

Figure 9: Static pressure distributions along the nozzle (effect of divergence angle for various throat diameters) (a): d_{th} = 0.5588 mm, (b): d_{th} = 3.175 mm.

It is concluded from the results that the flow at the nozzle throat is affected by the divergence angle. As the divergence angle increases, the flow reaches sonic conditions faster compared with a decrease in the divergence angle. This implies that the mass flow rate through the critical nozzle can change with the divergence angle.

4.6   Mass flux profiles

Figure (10) shows the mass flux profiles at the nozzle throat for P_o= 660 kPa with ρu_{theo} being the analytically-obtained mass flux. An adiabatic nozzle wall was assumed in the computation. In Fig. (10b) the effect of divergence angle on mass flux is found in the region below r/d_{th}= 0.45 for throat diameter 0.5588 mm. This coincides with to exit of the wall boundary layer, leading to a decrease in mass flux with a decrease in the divergence angle.

The skip in the mass flux profiles is observed close to the edge of the wall boundary layer. While the effect of the divergence angle is not largely found in a large throat diameter nozzle, see Fig. (10a), the skip is not formed in the mass flux profiles.
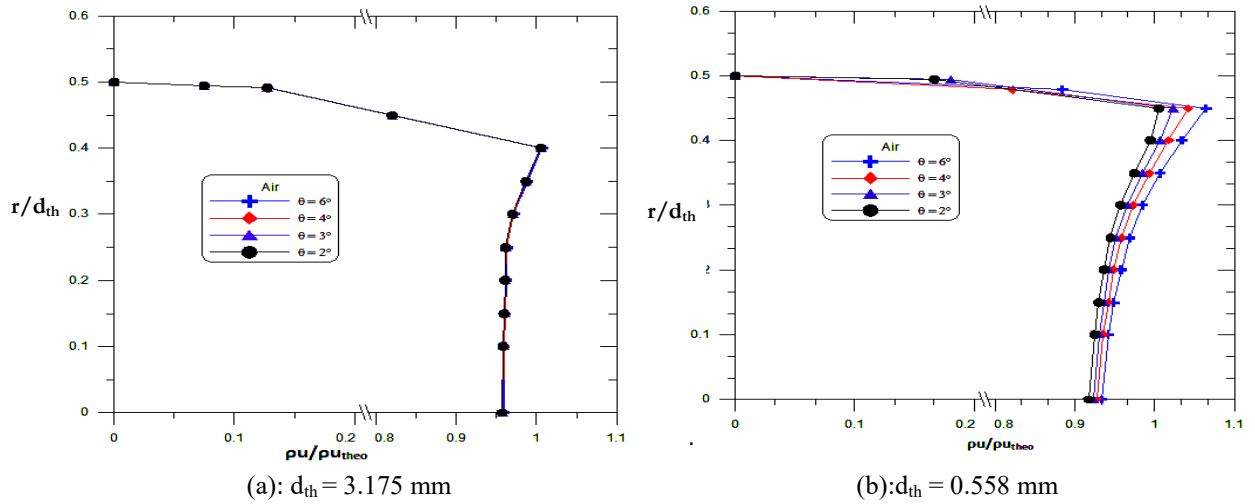
(a): d_{th} = 3.175 mm

(b): d_{th} = 0.558 mm

Figure 10: Mass flux profiles for nozzles with various throat diameters at P_o= 660 kPa

4.7 Flow field

As for the location of shock occurrence at different divergent angles see Fig. (11) at the back-pressure ratio of 0.6. Presents the Mach number contours for various divergence angles, indicating that the smaller the angle of the divergence, the closer the normal shock towards the nozzle exit.
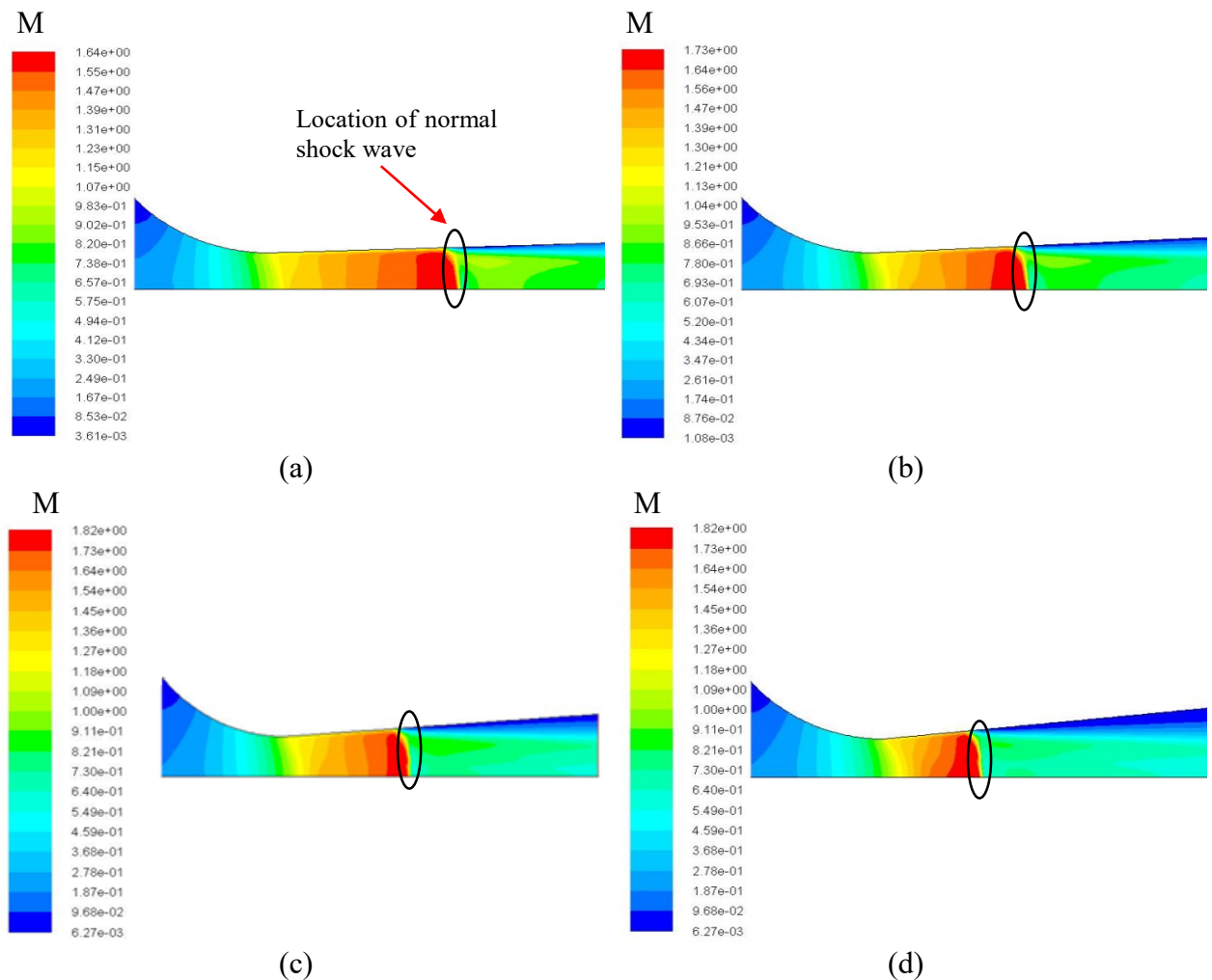

Figure 11: Mach number contours along sonic nozzle at ((a): θ= 2°, (b): θ= 3°, (c): θ= 4°, (d): θ= 6°).

4.8 Effect of back pressure ratio on working gas

Figure (12) shows the static pressure distribution along the sonic nozzle for different working gases and throat nozzle diameter equal to 3.175 mm and a back-pressure ratio of 0.2. The local static pressure continues decreasing with X/d_{th} and the inlet flow is subsonic up to sonic at the throat where it converts to supersonic thereafter. The dependance of the static pressure distribution on specific heat ratio is minute. For air, the specific heat ratio is 1.4, while that for methane is 1.3, so as the specific heat ratio increases, a decrease in static pressure occurs. While Fig. 13 explains the pressure distribution with different working gases in the case of a normal shock wave at a back-pressure ratio of 0.6, note that, in the beginning, the pressure ratio follows the same trend, then, after the throat happens, the pressure jumps as a result of the shock wave. Then, following that, it happens to have a drop in the back pressure that reaches the exit conditions. It also notes the normal-shock wave occurrence near the throat with the specific heat ratio increase.
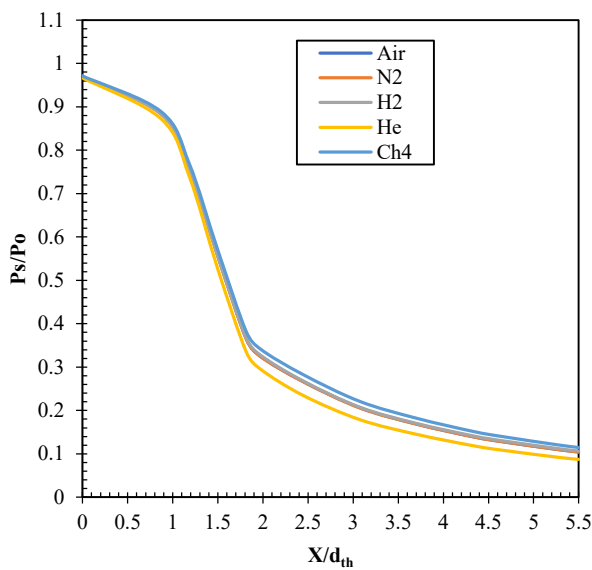

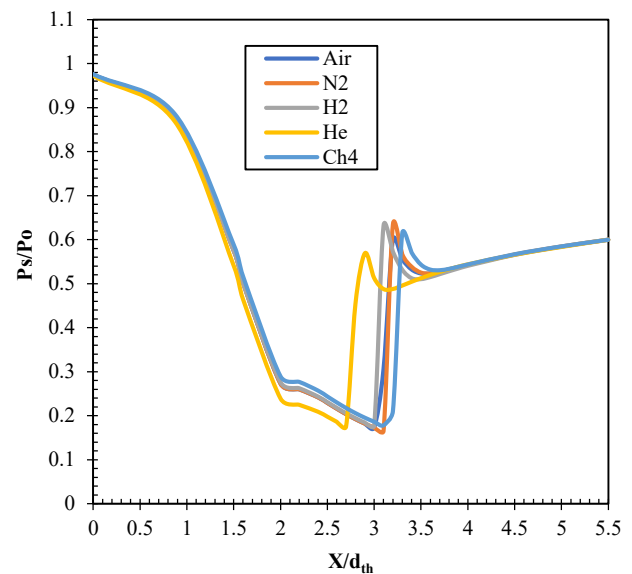**Figure 12:** Static pressure distribution of a long sonic nozzle for various gases (free flow gas).

Figure 13: Static pressure distribution of a long sonic nozzle for various gases (Normal shock wave).

4.9 Entropy change vs Mach number

The entropy increases with the Mach number increase for a nozzle with normal shock with different specific heat ratios as shown in Fig. (14). In the presence of a normal-shock wave, the boundary layer is very thin and the wall temperature before the shock is low and the velocity is very high. The effect of viscosity is important leading to entropy increase through a shock. Because the flow through the shock is adiabatic, stagnation temperatures before and after the shock are equal. However, due to increasing entropy, the stagnation pressure decreases across a normal shock.

4.10 Boundary layer

Figure (15) shows the boundary layer displacement thickness as a function of the Reynolds number according to eqn. (8). The boundary layer displacement thickness decreases with an increase in Reynolds number and vice versa. For H_2, the displacement thickness at the throat of the sonic nozzle reduces from 11μm to 4μm nearly at the same throat diameter of 3.175 mm when the Reynolds number increases from 6×10^4 to 4×10^5. Note that, the greater the molecular weight of the gas, the

greater the displacement thickness of the boundary layer. For the same Reynolds number, the boundary layer increase with the increased molecular weight of working gases. For the line shown in Fig. (15), at Re_d 2×10^5, the working gas changes from hydrogen to helium, and the displacement thickness of the boundary layer increase. This tendency is similar to the theoretical equation proposed by Gropp [11] as follows:

$$\frac{\delta}{d_{th}} = \frac{1}{\sqrt{Re_d.m}}\left[\frac{\gamma+1}{2}\right]^{\frac{1}{2(k-1)}}\left[3\sqrt{2}-2\sqrt{3}+\frac{\gamma-1}{\sqrt{3}}\right] \qquad (8)$$

Where γ specific heat ratio, m is a parameter dependent on the geometry of the sonic nozzle, defined as eqn. (9):

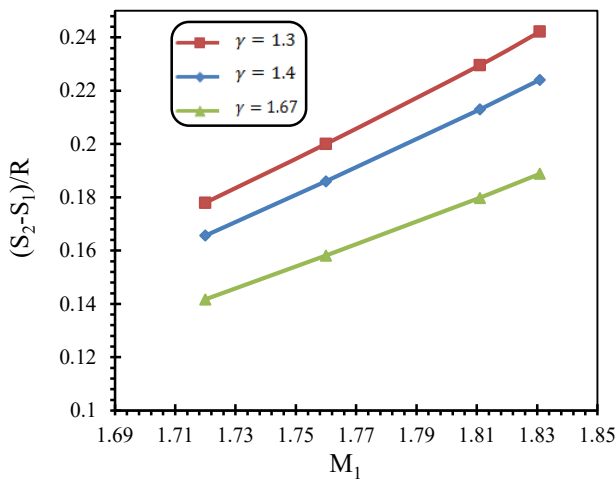$$m = \sqrt{\frac{2d_{th}}{R_c}\left(\frac{\gamma+1}{2}\right)^{\frac{3\gamma-1}{\gamma-1}}} \qquad (9)$$

Figure 14: Effect of Mach number before normal shock on entropy change for various gases.
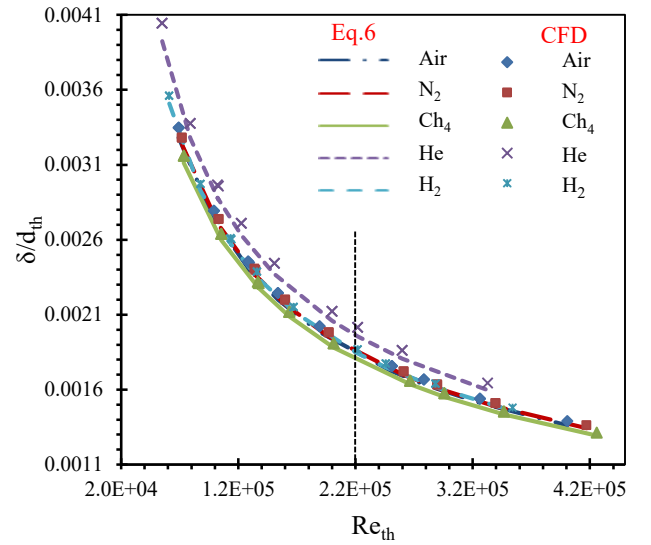

Figure 15: δ/d versus Re_{th}

Where d_{th} is the throat diameter and R_c is the radius of curvature. The present computational fluid dynamic results slightly overtake the boundary layer (δ) compared with the theoretical equation by Gerrop [11].

4.11 Performance map

Figure (16) shows a numerically-obtained performance map for a sonic nozzle operated under a normal shock wave in its divergent part. The map relates the Mach number downstream of the shock (M_2), the pressure ratio across shock (P_2/P_1), the temperature ratio across shock (T_2/T_1), the density ratio across shock (ρ_2/ρ_1), the entropy changes and the total pressure ratio, as dependent variables, to M_1 as a sole independent variable (parameter) for air being the working fluid. This independent variable is the Mach number upstream of the shock.

The map indicates that all dependent variables increase monotonically and almost linearly with M_1 except for M_2 and entropy change which are observed to decrease with M_1. It should be noted that the same map may be obtained experimentally but only expensively.
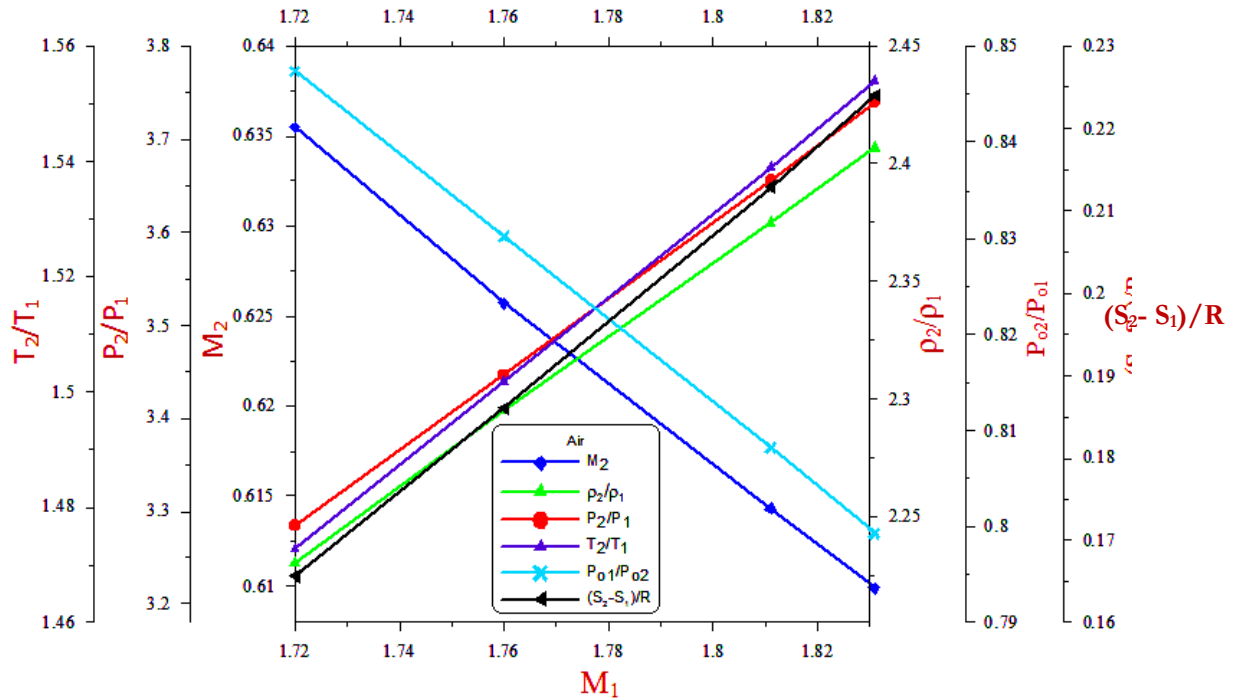
Figure 16: Numerically-based performance map for sonic nozzle under a normal-shock wave

5   Conclusion

This study aims to test the secondary standards sonic nozzle to find out the extent of their ability to prevent the effect of normal shock waves with various throat diameters and different divergence angles. It was concluded that the effect of divergence angle on mass flow rate across sonic nozzles plays an important role in avoiding normal shock occurrences. Looking at the results obtained, the following conclusions can be drawn:

- A good agreement was achieved between the experimental and simulation results. This is evidence of the compatibility of the boundary conditions used in the computational work.
- When there is an increase in divergence angle, there is an increase in the discharge coefficient due to an increase in the flow velocity and a decrease in boundary layer thickness. Normal shocks move toward the nozzle exit upon a decrease in divergence angle and an increase in throat diameter.
- It is possible to get a faster steady flow with an increased divergence angle and greater throat diameter with a constant back pressure ratio.
- For the nozzle throat diameter range from 0.558 to 3.175 mm and the back-pressure ratio is 0.6. The corresponding distance from the nozzle inlet toward the divergent section at which a normal shock occurs is 2.8 to 3.2.
- The normal-shock location with different working gases is dependent on a specific heat ratio for gas.
- The effect of divergence angle on mass flux is found in the region below $r/d_{th} = 0.45$ for throat diameter = 0.558 mm. However, larger critical nozzles show no effect on mass flow rate flux.
- The boundary layer displacement thickness increases with the greater molecular weight of the gas at the same Reynold number.

References

[1] Sutton, George Paul. History of liquid propellant rocket engines. *AIAA*, pp. 5-19, 2006.

[2] Nasuti, Francesco, and Marcello Onofri. "Shock structure in separated nozzle flows." *Shock Waves* vol. 19, no. 3, pp. 229-237, 2009. https://doi.org/10.1007/s00193-008-0173-7

[3] Choi, Hyun Ah, Ho Dong Kam, and Jeong Soo Kim. "Numerical Investigation On the Correlation Between Shock Structure and Thrust Performance in an Overexpanded Nozzle." 29th Congress of the International Council of the Aeronautical Sciences, September 7-12, 2014. http://icas.org/ICAS_ARCHIVE/ICAS2014/data/papers/2014_0948_paper.pdf

[4] Jae Hyung Kim, Heuy Dong Kim and Toshiaki Setoguchi. "The Effect of Diffuser Angle on the Discharge Coefficient of a Miniature Critical Nozzle." *Journal of Thermal Science*, vol. 19, pp. 222−227, 2010. https://doi.org/10.1007/s11630-010-0222-2

[5] Shaalan, M., F. Kassem, and R. Hagazy. "Calibration Nozzle Performance-State of The Art." *The Egyptian International Journal of Engineering Sciences and Technology (EIJEST)*, Vol. 26, pp. 1-13, 2018. doi: 10.21608/eijest.2018.97251

[6] Park, K. A., Choi Y M, Choi, H M, Cha, T S, Yoon. B., "The evaluation of critical pressure ratios of sonic nozzles at low Reynolds numbers". *Flow Measurement and Instrumentation*, vol. 12, pp. 37–41, 2001. https://doi.org/10.1016/S0955-5986(00)00040-6

[7] ISO 9300. "Measurement of Gas Flow by Means of Critical Flow Venturi Nozzles." 2nd edition, 2005E. https://www.sis.se/api/document/preview/906423/

[8] Masao Hayakawa, Yoshitaka Ina, Yoshikazu Yokoi, Masaki Takamoto, Shin-ichiNakao. "Development of a transfer standard with sonic Venturi nozzles for small mass flow rates of gases." *Flow Measurement and Instrumentation*, vol. 11, pp. 279–283, 2000. https://doi.org/10.1016/S0955-5986(00)00032-7

[9] Ke Han, Dong Luo, ShenYuming., "Numerical Simulation of the Internal Flow Field for the Straight Pipeline after a Sonic Nozzle and Its Influence on the Discharge Coefficient". *IEEE International Instrumentation and Measurement Technology*, pp. 9462 – 9465, 2016.   doi: 10.1109/ChiCC.2016.7554858

[10]Kim, H-D., J-H Kim, K-A Park, T Setoguchi and S Matsuo.,"Computational study of the gas flow through a critical nozzle." *J. Mechanical Engineering Science*, vol. 217, pp. 1179-1189, 2014. https://doi.org/10.1243/095440603322517180

[11]Geropp, D., "LaminareCrenzschichten in EbenenundRotationSsymmetrischenLavalduesen. Deutsche LuftundRaumfahrt for Schungsbericht"pp. 71–90, 1971.

[12]Arnberg, B. T., C. L. Britton, and W. F. Seidl. "Discharge coefficient correlations for circular arc venturi flow meters at critical (sonic) flow". *ASME 73-WA/FM-8*(1973). doi:10.1115/1.3447117

[13]Stratford, B. S., "The calculation of the discharge coefficient of profiled choked nozzles and the optimum profile for absolute air flow measurements." *J. R. Aeronaut. Soc*, vol. 68, pp. 237–245, 1962. https://doi.org/10.1017/S0001924000060905

[14]Liu, Yang, Xuewen Cao, Dan Guo, Hengguang Cao, and Jiang Bian. "Influence of shock wave/boundary layer interaction on condensation flow and energy recovery in supersonic nozzle." *Energy,* vol. 263, p. 125662, 2023. https://doi.org/10.1016/j.energy.2022.125662

[15] Dhandapani, Balasubramanian, and Jang-Chang Lee. "Study of divergence angle influence for sonic nozzle in non-equilibrium condensation." *Journal of Mechanical Science and Technology,* vol. 36, no. 6, pp. 2993-2999, 2023. DOI 10.1007/s12206-022-0531-x

[16] ANSYS Inc. ANSYS-Fluent User's Guide 14.5, 2012.

[17] Ishibashi, M.,and M .Takamoto. "Theoretical discharge coefficient of a critical circular-arc nozzle with laminar boundary layer and its verification by measurements using super-accurate nozzles."*Flow Measurement and Instrumentation,* vol. 11, pp. 305-313, 2000. https://doi.org/10.1016/S0955-5986(00)00029-7